Article

An Assessment of SNPP and NOAA20 VIIRS RSB Calibration Performance in NASA SIPS Reprocessed Collection-2 L1B Data Products

Aisheng Wu [1],*, Xiaoxiong Xiong [2], Rajendra Bhatt [3], Conor Haney [4], David R. Doelling [3], Amit Angal [1] and Qiaozhen Mu [1]

[1] Science Systems and Applications, Inc., 10210 Greenbelt Rd, Lanham, MD 20706, USA
[2] Sciences and Exploration Directorate, NASA Goddard Space Flight Center, Greenbelt, MD 20771, USA
[3] NASA Langley Research Center, Hampton, VA 23666, USA
[4] Science Systems and Applications, Inc., Hampton, VA 23666, USA
*   Correspondence: aisheng.wu@ssaihq.com

Abstract: Two VIIRS sensors onboard the SNPP and NOAA20 satellites have been successfully operating for over 10 and 4 years, respectively, providing the worldwide user community with high-quality imagery and radiometric measurements of the land, atmosphere, cryosphere, and oceans. This study provides a temporal radiometric stability and calibration consistency assessment of the SNPP and NOAA20 VIIRS reflective solar bands using the latest NASA SIPS C2 L1B products. Several independent vicarious approaches are used to examine the stability of SNPP VIIRS and consistency of the at-sensor reflectance between the two VIIRS instruments. These approaches include observations from simultaneous nadir overpasses, the Libya-4 desert and Dome C snow/ice sites, and deep convective clouds. The impact of existing band spectral differences on the reflectance measurements is accounted for utilizing scene-specific hyperspectral observations provided by the SCIAMACHY sensor onboard the ENVISAT platform. Results indicate that both SNPP and NOAA20 VIIRS reflectances are stable within 1% over their mission periods for all bands, except for a few bands in the visible range from SNPP VIIRS that show more upward drifts at high radiances. NOAA20 VIIRS reflectances are systematically lower than SNPP by 2 to 4% for most bands, with the exception of few short wavelength bands where it is seen to be up to 7%.

Keywords: VIIRS; reflective solar bands; reflectance; vicarious calibration

1. Introduction

Two Visible Infrared Imaging Radiometer Suite (VIIRS) sensors onboard the Suomi National Polar-Orbiting Partnership (SNPP) and NOAA20 satellites have been successfully operating for over 10 and 4 years, respectively, providing imagery and radiometric measurements of the Earth to generate various products in the study of the land, atmosphere, cryosphere, and oceans [1–3]. Both satellites are in the afternoon orbit with an equator crossing time of 1:30 PM. VIIRS has 22 spectral bands with wavelengths ranging from 0.41 to 12.0 μm, including 14 reflective solar bands (RSB), 7 thermal emissive bands, and 1 day–night band (DNB). The VIIRS sensor was built with a strong Moderate Resolution Imaging Spectroradiometer (MODIS) heritage, with a wider swath range (3000 km versus 2330 km), a more consistent spatial resolution across the entire scan due to a unique pixel aggregation, and a wider dynamic range from the dual-gain setting, particularly suitable for ocean color applications. VIIRS is equipped with a rotating telescope assembly (RTA) instead of a scan mirror that was used in MODIS. Major advantages of RTA include a smaller angle of incidence (AOI) range relative to the half angle mirror (HAM) and less exposure to degradation because of the presence of multiple mirrors in the RTA system, effectively blocking most of the UV radiation [4,5].

The calibration of the VIIRS RSB relies on a solar diffuser (SD), with a solar attenuation screen and a solar diffuser stability monitor (SDSM) as the primary calibration source. During the first few months after launch of both SNPP and NOAA20 VIIRS sensors, a series of instrument yaw maneuvers were scheduled to improve the SDSM and SD screen transmission functions that were derived based on prelaunch tests [6–9]. The VIIRS lunar measurements are used as a supplemental calibration source based on the methodology that was originally developed for the two MODIS instruments [10]. The use of lunar data was first employed in SNPP VIIRS and later extended to NOAA20 VIIRS. The VIIRS Moon and SD views are fixed at the same AOI (60.2°) for the RTA HAM. The benefit of having two independent sources at the same AOI for VIIRS provides a good opportunity to validate and improve the SD-based calibration results.

Compared with NOAA20 VIIRS, there are a few major changes and updates in the SNPP VIIRS RSB calibration algorithm made by the NASA VIIRS Characterization Support Team (VCST) over the mission. A unique calibration issue related to SNPP VIIRS is related to wavelength-dependent degradation in the near-infrared (IR) to SWIR wavelength region, which is due to RTA mirror coating issues during the manufacturing process [11]. Although the degradation due to this anomaly is up to 45% in the gain, it is well captured by the onboard SD/SDSM measurements and impact on the calibrated radiance/reflectance is negligible. The accelerated gain degradation in the near-IR and SWIR wavelength region has an impact on the relative spectral response (RSR), particularly in the early months of the mission. As a result, a time-dependent, modulated RSR is applied to capture the degradation impact [12]. SNPP VIIRS lunar calibration measurements have been used to support its RSB on-orbit calibration to track their long-term stability. Although there are noticeable seasonal variations in the lunar measurements, their trends are consistent with those derived from the SD measurements. With cumulative lunar data for multiple years, it is possible to detect changes of significantly lower than 1% over time in the calibration of the VIIRS RSB [13,14]. In addition to the use of on-board calibration and lunar measurements, Earth view (EV) imagery also provides an effective way to assess the quality of the calibration performance. Examination of the EV images over the Libya-4 desert site and deep convective clouds (DCC) showed that image striping gradually increases with time, with a radiometric impact of less than 0.7% early in the mission to more than 2% in recent years, particularly in the shortest wavelength bands [15,16]. The image striping is likely attributed to the spatially non-uniform degradation of the SD, which causes a detector-dependent calibration error. A de-striping approach based on the results from the EV data is applied to the SNPP VIIRS calibration algorithm. As a result, there was a reprocessed version of the SNPP VIIRS Level 1B (L1B) product, generated by NASA Land SIPS (Science Investigator-led Processing Systems). In contrast, the NOAA20 VIIRS instrument has been very stable since launch. This is mainly because the on-orbit changes in gain are within 0.5%. Currently, Collection-2 (C2) represents the latest operational and publicly available version of the NASA SIPS VIIRS Level-1B products for SNPP and C2.1 for NOAA20. All the changes made in the calibration algorithm discussed above are included in the C2 L1B products, which were reprocessed starting on 14 November 2020 and 27 January 2021, respectively.

The objective of this study is to provide a complete assessment of SNPP and NOAA20 RSB calibration performance and consistency based on NASA SIPS C2 L1B products. Initial results of the calibration consistency between the two sensors for selected RSB were reported in our early studies after applying the scaling factors for the gain from C1 to C2 [17]. Results indicate NOAA20 reflectances are systematically lower than SNPP by 2% to 4% for most RSB and a few of the shortest wavelength bands show even larger differences. Similar studies have been conducted using a VIIRS sensor data record (SDR) obtained from the NOAA Comprehensive Large Array-Data Stewardship System (CLASS) [18,19]. These studies indicate the NOAA20 VIIRS measured top-of-atmosphere (TOA) reflectance is consistently lower than that of the SNPP on the order of 2% to 4%. Compared with SIPS L1B, there are temporal inconsistencies during early mission years in the radiometric

calibration of the SNPP VIIRS SDR products generated by NOAA CLASS. In addition, the NOAA SDR calibration team and NASA VCST applied their independent calibration algorithms with differences in the fitting approach for the SNPP lunar/SD trends. This study provides a complete assessment of the VIIRS RSB radiometric stability and consistency over the mission for both SNPP and NOAA20 using the NASA SIPS VIIRS products. We apply the approaches that were used in our earlier studies to assess the MODIS and VIIRS calibration performance including the simultaneous nadir overpass (SNO), pseudo-invariant calibration sites (PICS), such as Libya-4 desert and Dome C and deep convective clouds (DCC) [20–22]. One reason that there is an emphasis on NOAA20 VIIRS is because it has shown more stable on-orbit performance than SNPP VIIRS. In addition, the global Space-based Inter-Calibration System (GSICS), an international organization dedicated to providing consistent calibration among operational satellite sensors, has recommended replacing Aqua MODIS with NOAA20 VIIRS as an absolute calibration reference [23]. Since Aqua MODIS has continued to operate with more than a decade beyond its design life, the transfer of the calibration reference from Aqua-MODIS to NOAA20 VIIRS appears necessary to ensure a consistent retrieval product across more recent and future sensors. Calibration performance issues discussed in this study can also provide useful information for better understanding and further improvement of downstream products that involve the use of VIIRS observations.

2. Method

2.1. Instrument Background

The VIIRS sensor is a whiskbroom scanning radiometer with multiple spectral bands covering a wavelength range from 0.41 to 12.0 μm. The RTA and HAM assembly is used to scan over the Earth [4,6]. Images of the Earth scenes are taken at two spatial resolutions: 375 m for the higher resolution "I" bands and 750 m for the moderate resolution "M" bands. Pixels are aggregated proportionally in the along-scan direction to reduce the impact of the increase in pixel size toward the end of scan (the bow-tie effect) due to the Earth's curvature. There are 14 bands for RSB (I1-I3 and M1-M11) and 7 for the thermal emissive bands (I4-I5 and M12-M16) and a unique DNB at 750 m resolution. Among the 22 bands, there are 7 dual-gain bands: M1-M5, M7, and M13. For these bands, the electronics can switch between high gain and low gain modes in the on-board signal processing based on the observed signal level, which significantly increases the dynamic range in Earth scene observations. The VIIRS bands are located on three focal planes (FPAs) depending on the wavelength: visible (VIS) and near-infrared (NIR), short- and mid-wave infrared (S/MWIR), and long-wave infrared (LWIR). The S/MWIR and LWIR FPAs are cooled to a temperature of approximately 80 K, while the VIS/NIR FPA is operated at the sensor's ambient temperature. Table 1 provides a summary of VIIRS spectral bands and key design requirements for RSB. The requirements for VIIRS RSB radiometric calibration uncertainties are ±2% in reflectance and ±5% in radiance [7].

2.2. Libya-4 Site

To evaluate the calibration performance and consistency of SNPP and NOAA20 VIIRS RSB, various vicarious approaches that utilize Earth scene observations are used [17–19]. The first approach is based on reflectances collected over the widely used Libya-4 desert site (28.5° N, 23.4° E) [20–22]. We choose near-nadir overpasses with view zenith angles less than 5° over the site, obtained from 16-day repeatable orbits. This provides trends of reflectance with nearly identical view zenith angles close to the nadir, making it easier to mitigate bidirectional reflectance effects. Data are extracted on a 25 km × 25 km area surrounding the site at the pixel level and averaged for each band and HAM side. A pre-defined criteria (standard deviation from the mean <2%) to examine the uniformity of the extracted pixels is used to exclude cloudy contamination. Any overpasses over the site with the standard deviations larger than the criteria are excluded. Since the local equatorial crossing times are nearly the same, the view and solar zenith angles of the

site from the two VIIRS sensors are in a similar angular range. A site-dependent semi-empirical bi-directional reflectance function (BRDF) model based on measurements from SNPP VIIRS is applied to the reflectances derived from the spectrally matching bands. The BRDF normalized reflectances are used to track the stability and make the cross-sensor comparison. The BRDF model is based on the semi-empirical kernel-based formulation provided by Roujean et al. [24] as expressed below

$$R^i(\theta, \phi, \psi) = K_0^i + K_1^i f_1(\theta, \phi, \psi) + K_2^i f_2(\theta, \phi, \psi) \tag{1}$$

where R is the anisotropic reflectance factor, θ, φ and ψ are the solar zenith, view zenith, and relative azimuth angles, i is the index for the band wavelength, f_1 is derived from volume scattering component, while f_2 is the component from surface scattering and geometric shadow casting theory. Details about formulation of f_1 and f_2 can be found in the reference. Coefficients K^i_0, K^i_1, and K^i_2 are given as functions of parameters related to the physical structure and optical properties of a reflecting surface in the original model. To the first approximation, it can be assumed that K^i_0, K^i_1, and K^i_2 are surface type-specific and they are derived from multilinear regression using cumulative SNPP data over the initial three-year period to cover the seasonal cycle of the angular parameters. The BRDF correction based on the SNPP coefficients is applied to both sensors. Our previous studies [17,25] showed that by restricting view zenith angles to a narrow range, the BRDF model can reduce the impact of a seasonal cycle to within 1% in temporal variation post correction for bands in the visible and infrared region. In the case of the bands in the shortwave infrared (SWIR) region, however, there are a few exceptions with a slightly large temporal variation (>1%) for some SWIR bands (i.e., 1.3 μm), which have a low signal level or a high sensitivity to atmospheric water vapor over Libya-4.

Table 1. A summary of spectral characteristics (in μm), typical radiance (in W/m^2/μm/Sr), signal to noise ratio (SNR) and noise equivalent temperature difference (NEdT; in K), and the primary purposes of each SNPP VIIRS band. The SNR are based on pre-launch measurements and three on-orbit time periods. The NOAA20 band M11 values are shown in parenthesis.

Band	Wavelength (μm)	Bandwidth (μm)	Gain Mode	Ltyp	SNR Spec.	Primary Use
I1	0.64	0.08	Single	22	119	Imagery
I2	0.865	0.039	Single	25	150	Imagery
I3	1.61	0.06	Single	7.3	6	Imagery
M1	0.412	0.02	Low/High	44.9/155	352/316	Ocean Color, Aerosol
M2	0.445	0.018	Low/High	40/146	380/409	Ocean Color, Aerosol
M3	0.488	0.02	Low/High	32/123	416/414	Ocean Color, Aerosol
M4	0.555	0.02	Low/High	21/90	362/315	Ocean Color, Aerosol
M5	0.672	0.02	Low/High	10/68	242/360	Ocean Color, Aerosol
M6	0.746	0.015	Single	9.6	199	Atmospheric corr'n
M7	0.865	0.039	Low/High	6.4/33.4	215/340	Ocean Color, Aerosol
M8	1.24	0.02	Single	5.4	74	Cloud optical thickness over snow/ice
M9	1.378	0.015	Single	6	83	Cirrus/Cloud Cover
M10	1.61	0.06	Single	7.3	342	Snow Fraction
M11	2.25	0.05	Single	0.12 (1)	10 (90)	Clouds

2.3. Dome C Site

The second approach is based on reflectances collected over the Dome C ice/snow site (75.1° S, 123.4° E) on the Antarctic Plateau, one of the most homogeneous land surfaces

uniformly covered by snow and icesheets [26]. Since VIIRS is in a polar orbit, this approach has advantages of more frequent overpasses over the polar region (during local summer) than the Libya-4 desert site. There is approximately one near-nadir overpass per day available during the Antarctic summer period. Similar to the Libya-4 approach, an average of reflectance collected over a 25 km × 25 km area centered at the Dome C site is calculated. Pre-determined spatial standard deviations of 1% for the pixel window are used to remove overpasses due to a possible cloud impact. Early studies showed that a simple BRDF model expressed as a linear relationship with solar zenith angle works reasonably well, as shown in Figure 1, and is applied to the Dome C reflectance data [27,28]. The BRDF model reduces the angular dependent fluctuations to within 1% for the short wavelength visible bands and 1–2% for the remaining bands with longer wavelengths. In the case of the SWIR bands, results from the Dome C site are significantly noisy due to either a low signal level or high sensitivity to atmospheric conditions. Due to concern about large uncertainties in the Dome C SWIR band results, they are not included in this study.
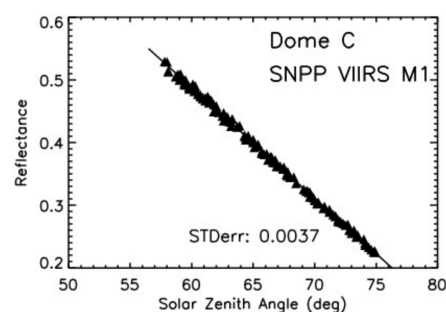

Figure 1. Relationship between L1B reflectance and solar zenith angle for SNPP VIIRS M1 (0.412 μm) over the Dome C site. Each point represents one overpass and data are collected from the initial three years of the mission. A linear regression line is shown in the figure.

2.4. SNO

The third approach is based on SNO that provides a direct pixel level comparison between two crossover sensors. Since there is no simultaneous crossover between SNPP and NOAA20 satellites, a third sensor, Aqua MODIS, is used as a transfer radiometer [29,30]. A double difference method is used to make a comparison of SNPP and NOAA20 VIIRS. There is an abundance of VIIRS and MODIS SNOs, with nearly one SNO event every three days. The frequent locations of these SNOs are in the high-latitude region. The SNO data sets collected in this study are from the MODIS and VIIRS crossovers with a less than 30 s time difference between the two. A further restriction of the SNO areas is to limit the distance between the nadirs of the two sensors to within 100 km. An averaged ratio of reflectance between VIIRS and MODIS is determined once a statistically sufficient sample size (~30,000 matched pixel pairs) is obtained from each SNO. The impact of the pixel footprint difference between MODIS (1 km) and VIIRS (750 m) on the averaged ratio can be significant over highly inhomogeneous surfaces. Similar to Libya-4 and Dome C sites, pre-defined standard deviations are applied for data quality control to exclude the SNO events with the standard deviations beyond the limitation. The reason that the matched VIIRS and MODIS data are extracted at the pixel level is due to consideration of avoiding saturated pixels in the MODIS high-gain bands, which are mainly used in the retrieval of ocean color products. This allows more VIIRS bands to be used in the SNO approach. The majority of the SNO match ups occur around latitude 70° north or south across multiple scene types and locations. Since there is no restriction of SNO on location and surface type, results of this approach contain data from a wide variety of scene types. Figure 2 shows a typical example of pixel-to-pixel comparison of reflectance at 0.44 μm between SNPP VIIRS M1 and Aqua MODIS band 8 based on a SNO event from 7 October 2021
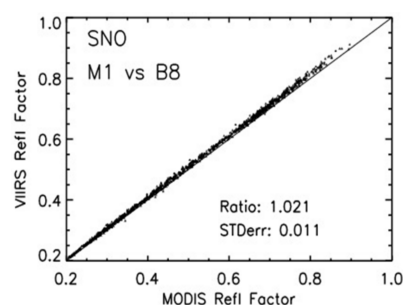
Figure 2. Example of pixel-to-pixel comparison of reflectance between SNPP VIIRS M1 and Aqua MODIS band 8 obtained from one SNO event at 21:48 GMT on 7 October 2021. The pixel matchup is determined from the center-to-center distance (<350 m) between VIIRS and MODIS. Numbers shown in the figure are values of the averaged VIIRS to MODIS reflectance ratio and standard error.

2.5. DCC

Tropical deep convective clouds (DCC) are some of the most promising Earth invariant targets for post-launch radiometric calibration of satellite imagers. Compared to ground PICS, they offer high signal-to-noise ratio in most of the reflective solar wavelength range, are significantly less affected by atmospheric water vapor column, and have a nearly Lambertian reflectance characteristic in the visible and near-infrared solar spectrum [31,32]. The baseline DCC method is a large-ensemble statistical approach that relies on the assumption that the distribution of DCC reflectance in the visible spectrum remains constant in time. The method uses an 11-μm infrared (IR) channel brightness temperature (BT) threshold of 205 K to identify the DCC pixels over the tropics. A spatial homogeneity filter is applied in the visible (VIS) reflectance and IR BT measurements by computing the spatial standard deviation (σ) of a 3 × 3 pixel block surrounding the DCC pixel target to eliminate the optically thin clouds. Pixels with σ less than 3% in VIS (0.64 μm) and 1 K in IR are used. The DCC pixel level reflectance values are compiled into monthly probability distribution functions (PDF). Prior to the construction of the PDF, the baseline DCC method applies anisotropic corrections to the DCC pixels using the angular distribution model (ADM) derived by Hu et al. [33]. The statistical mode of the monthly PDFs is computed and tracked over time as a means for monitoring the sensor stability (Figure 3). Previous studies [31,32] have shown that the Hu ADM is effective in mitigating the bidirectional reflectance effects in DCC pixel reflectance values in the visible and near-infrared (VIS-NIR) bands (<1 μm). The observed temporal natural variability of the monthly PDF mode timeseries in VIS-NIR wavelengths is below 1%. However, at shortwave infrared (SWIR) wavelengths (>1 μm), the DCC reflectivity is affected by ice particle size [34]. With an increase in the ice effective diameter, the single scattering albedo decreases, which results in an increased absorption or, equivalently, reduced reflected solar energy at top of the atmosphere. Compared to VIS-NIR wavelengths, the DCC SWIR reflectance exhibits a greater dependence on wavelength, and an increased sensitivity to viewing and solar illumination geometry, and the brightness temperature threshold. Recently, Bhatt et al. [35,36] revised the baseline DCC calibration method to extend its application to SWIR bands. The revised approach relies on the seasonal characterization of the DCC bidirectional reflectance at multiple SWIR wavelengths utilizing first 5 years of DCC measurements taken from the SNPP VIIRS SWIR bands. The DCC BRDF features found are unique for each of the VIIRS SWIR bands, thereby suggesting that a wavelength specific BRDF is essential when employing the DCC method for SWIR bands. This study utilizes the Hu ADM and the SNPP VIIRS based channel-specific empirical BRDF models for anisotropic corrections of the DCC pixel level reflectance values in VIS-NIR and SWIR bands, respectively. In addition, the monthly mean DCC reflectance is preferred over the mode statistics for SWIR bands. The application of the empirical BRDF models can effectively reduce the temporal variability in the SWIR band DCC response and, consequently, allow for detection of a gradual sensor trend of magnitude as low as 0.7%/decade at the 5% significance level (or 95% confidence level) [35].
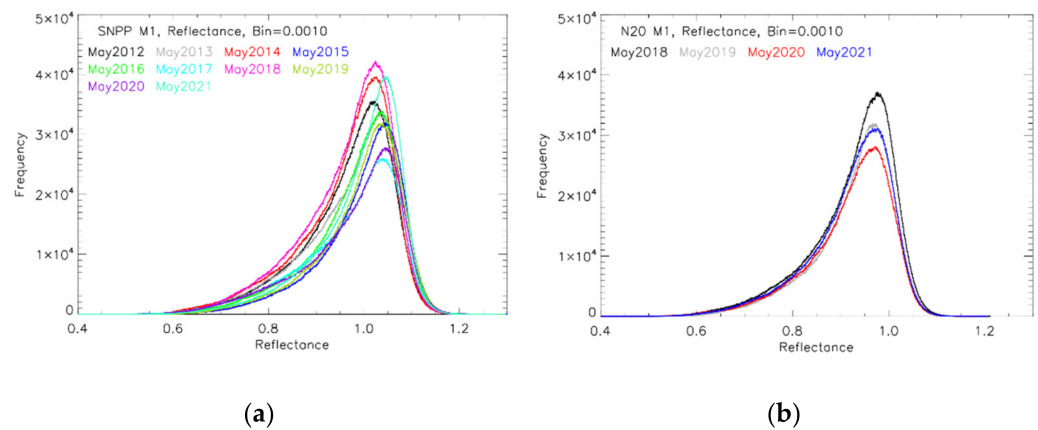
(**a**) (**b**)

Figure 3. Monthly DCC PDF in reflectance for SNPP (**a**) and NOAA20 (**b**) VIIRS M1 band. The month of May each year is selected for the two VIIRS sensors, respectively.

2.6. Correction for Spectral Differences

There are existing differences in the relative spectral response (RSR) between SNPP and NOAA20 RSB that affect the radiometric assessment between the two sensors. The correction is expressed as a ratio of NOAA20 to SNPP reflectance, $R^{N20/SNPP}$, determined using hyperspectral observations

$$R^{N20/SNPP} = \frac{\sum_{i=0}^{t\_N20} \rho_{SCIA,i} RSR_{N20,i}(\lambda_{N20,i} - \lambda_{N20,i-1})}{\sum_{i=0}^{t\_N20} RSR_{N20,i}(\lambda_{N20,i} - \lambda_{N20,i-1})} \Big/ \frac{\sum_{j=0}^{t\_SNPP} \rho_{SCIA,j} RSR_{SNPP,j}(\lambda_{SNPP,j} - \lambda_{SNPP,j-1})}{\sum_{j=0}^{t\_SNPP} RSR_{SNPP,j}(\lambda_{SNPP,j} - \lambda_{SNPP,j-1})} \tag{2}$$

where $\rho_{SCIA,i}$ and $\rho_{SCIA,j}$ are the hyperspectral measured spectral reflectances at wavelength bins i and j, respectively, $RSR_{N20,i}$ and $RSR_{SNPP,j}$ are the NOAA20 and SNPP spectral responses at wavelength bins i and j, and t_N20 and t_SNPP are the total number of wavelength interval for NOAA20 and SNPP, respectively. When using Aqua MODIS as a transfer radiometer in the SNO approach, a ratio of $R^{N20/Aqua}$ and $R^{SNPP/Aqua}$ is used to determine $R^{N20/SNPP}$. The hyperspectral observations are based on early data obtained from SCIAMACHY, one of ten instruments aboard ESA's Environmental Satellite, ENVISAT [37]. The SCIAMACHY sensor provides measurements with a relatively high spectral resolution of 0.2 to 0.5 nm and covers a wide wavelength range from 240 to 1700 nm. Although the ENVISAT mission ended on 9 May 2012, it provides a decade-long global dataset from August 2002 to April 2012. The hyperspectral L1B data (SCI_NL_1P, version 7.03) over a one-year period in 2004 are analyzed for this study. Information on the scene identification for the Libya-4 and Dome C approaches is based on geolocation. For the reflectances from the SNO approach, since the data locations are not fixed, averaged SCIAMACHY overpasses over the various surfaces are used. The time-independent $R^{N20/SNPP}$ correction is a single factor that depends on spectral band and surface type in the Libya-4, Dome C, and SNO approaches (Table 2). For the DCC approach, the impact of the band spectral difference is estimated based on the SCIAMACHY-based spectral band adjustment factor (SBAF) tool provided by NASA-LaRC (see link at https://cloudsgate2.larc.nasa.gov/cgibin/site/showdoc?mnemonic=SBAF) (accessed on 15 April 2022) [38]. In addition to the impact due to the spectral differences, the continuous on-orbit spectral degradation in the SNPP VIIRS RTA mirror reflectance causes a change in the spectral shape of RSR. It also changes the relative contribution of out-of-band signal to the total. However, impact on most RSB is less than 0.1% in general. VIIRS M1 shows a larger difference of 0.25%, which is primarily due to contribution from its relatively large out-of-band response [39].

Table 2. The RSR correction between SNPP and NOAA20 VIIRS RSB derived using Equation (1) for the four vicarious approaches. Note results for M11 are based on Hyperion data for DCC and MODTRAN simulations for other approaches.

Band (μm)	M1 0.412	M2 0.445	M3 0.488	M4 0.555	M5 0.672	M7 0.865	M8 1.24	M9 1.378	M10 1.61	M11 2.25	I1 0.640	I2 0.865	I3 1.61
Libya-4	1.004	1.012	0.996	1.019	1.000	0.994	1.001	NA	0.999	0.990	1.002	0.992	0.997
DCC	1.000	1.008	1.000	0.994	1.001	0.998	1.000	1.001	1.013	0.992	1.003	0.996	1.015
Dome C	1.015	1.013	0.994	0.983	1.002	0.978	0.993	NA	1.017	0.988	0.992	0.979	0.999
SNO	1.013	1.012	0.993	0.989	1.001	0.990	1.000	1.003	1.001	0.993	0.995	0.986	0.999

Each of the above-described approaches has distinct advantages and disadvantages. The Libya-4 site has been frequently used for sensor calibration performance monitoring. This site provides an excellent spatial and temporal stability with an optimum signal level of the reflected sunlight that makes it very useful to the Earth observation community. There are a few disadvantages, including impact of cloudy conditions and uncertainties associated with atmospheric absorption. The Dome C site is of interest for calibration due to its spatial homogeneity. The atmospheric conditions are dry and clear most of the time because of its high elevation. In addition, due to its location in Antarctica, the site is more frequently observed by polar orbiting satellites. The main disadvantage is the impact of high solar zenith angles (>50°), which magnify the BRDF impact, and useful sunlit observations occur only for 4 useful months out of the year. The SNO approach has been proven to be very effective in conducting sensor intercomparison. Impacts due to Earth scene variations and effects of the BRDF are largely reduced because observations are made over the same surface target and at nearly the same time for the spectrally matched bands of a given pair of instruments. The main limitation of the SNO approach is that it is only applicable near the polar region with observations obtained from scenes with a unique surface and cloud conditions. For the stability analysis, the SNO must rely on the stability of the reference sensor to monitor the stability of the target sensor. Since the surface spectral characteristic changes with location, any spectral mismatch between the two instruments would require a surface type dependent correction. The advantage of the DCC approach is that DCC are abundant and located at the tropopause level, where the effects of atmospheric absorption are significantly reduced. They are extremely bright earth targets with a nearly Lambertian reflectance. This approach has been successful in visible and near-infrared bands. However, unlike the other three approaches, it requires a large ensemble statistical technique to derive a stable result. Saturation over DCC limits is use for many MODIS RSB; but, in the case of VIIRS, it has six dual-gain RSB bands that have a wide enough dynamic range to avoid saturation over any Earth scenes.

3. Results

Trends of near-nadir reflectance for the SNPP and NOAA20 VIIRS M3 (0.488 μm) band obtained from the four vicarious approaches are shown in Figure 4. For the Libya-4 and Dome C approaches, a site-dependent BRDF model derived using SNPP VIIRS reflectance data is applied to both sensors. For the DCC approach, the anisotropic correction is applied to DCC pixels using the Hu model [33]. For the SNO approach, no BRDF corrections are implemented as the Aqua MODIS is used as a transfer reference. Because of the use of the BRDF correction, the SNPP reflectance trends for the first three approaches are normalized to 1 at the beginning of the mission. Results indicate that both SNPP and NOAA20 VIIRS are stable, although the operational period for NOAA20 is just over 4 years. For SNPP VIIRS, a 10-year cumulative data set provides a good quantitative stability assessment. It should be noted that the stability assessment from the SNO approach is a combined result from VIIRS and MODIS. The combined standard errors from the SNPP and NOAA20 for the DCC approach are the lowest among the four approaches in the visible region due to its high uniformity and nearly Lambertian reflection distribution for a large range of

solar zenith and viewing zenith angles. For SNPP, trends from DCC and Dome C site show an upward drift of more than 1.0%, compared with a slightly downward trend for the Libya-4 site. Examination of the stability results for all SNPP VIIRS RSB indicates there is an upward drift in the DCC and Dome C results for bands M1 to M5. The drift manly occurs early in the mission before 2014, with the largest magnitude observed in M3.
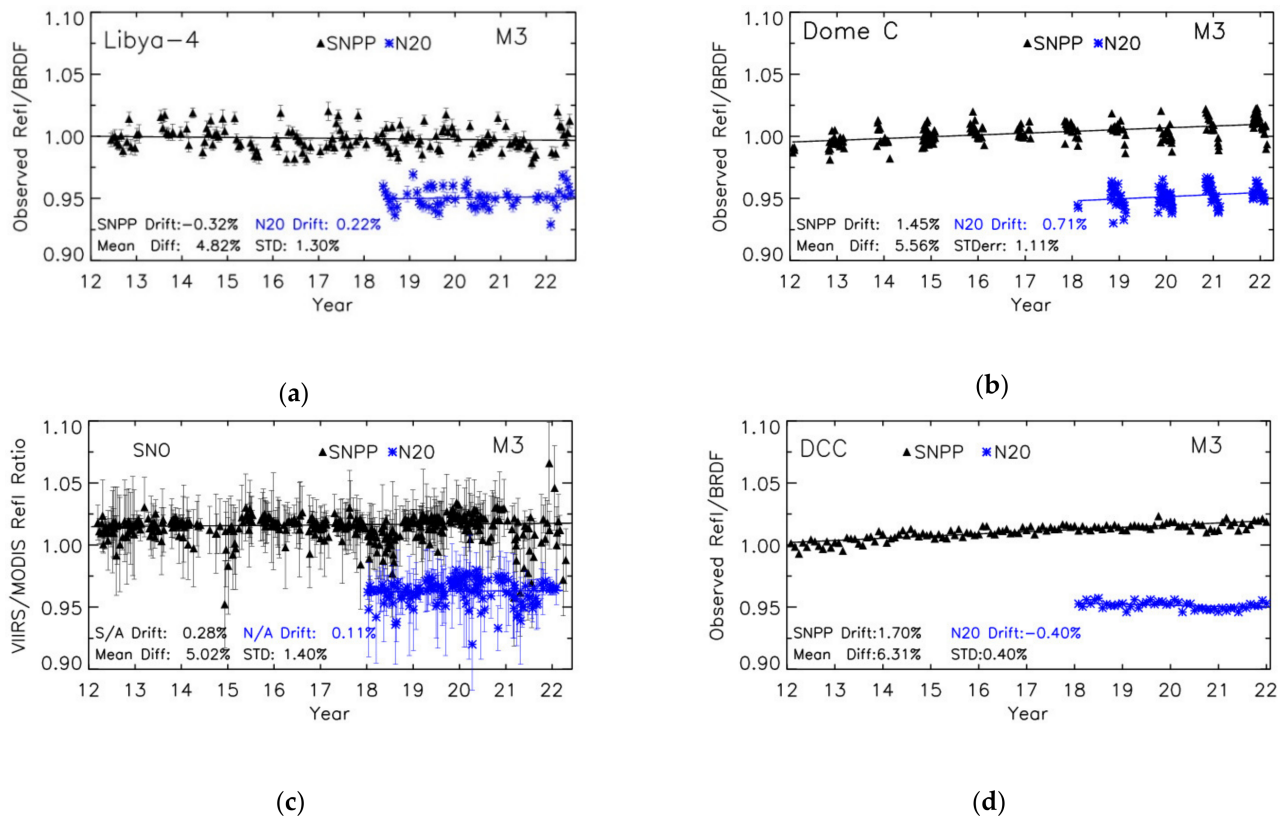

(**a**)

(**b**)

(**c**)

(**d**)

Figure 4. Normalized reflectance trends for SNPP and NOAA20 VIIRS M3 obtained from the Libya-4 (**a**), Dome C (**b**), SNO with Aqua MODIS (**c**), and DCC (**d**).

Comparing the normalized reflectances between SNPP and NOAA20 for their overlapping period provides an assessment of the relative consistency for radiometric calibration. Additional factors affecting the systematic biases include differences in spectral response, atmospheric effect, etc. Comparison of results indicates NOAA20 reflectances are systematically lower than SNPP by approximately 5–6% before correcting their existing spectral differences. As previously discussed, results from other bands also confirm that NOAA20 reflectances are systematically lower than SNPP.

Figure 5 shows trending results for VIIRS M7 (0.865 μm). Compared with results of M3 in the VIS wavelength for the Dome C site, the standard errors are significantly increased. Examination of the fitting residuals of the Dome C BRDF indicates this is due to inadequacy of the BRDF for bands with longer wavelengths. No significant improvement was found by replacing the simple linear BRDF model that is currently used for the Dome C site with more complex models, such as the semi-empirical model applied to the Libya-4 site. In terms of stability, results from the near-IR bands are stable to within 1% and consistent among the four approaches. Similar to the results from the VIS bands, the combined standard errors for the DCC approach are the lowest among the four approaches. The magnitudes of the difference are approximately 4%, compared with 5–6% for the VIS bands, indicating a wavelength-dependent bias between the two sensors.
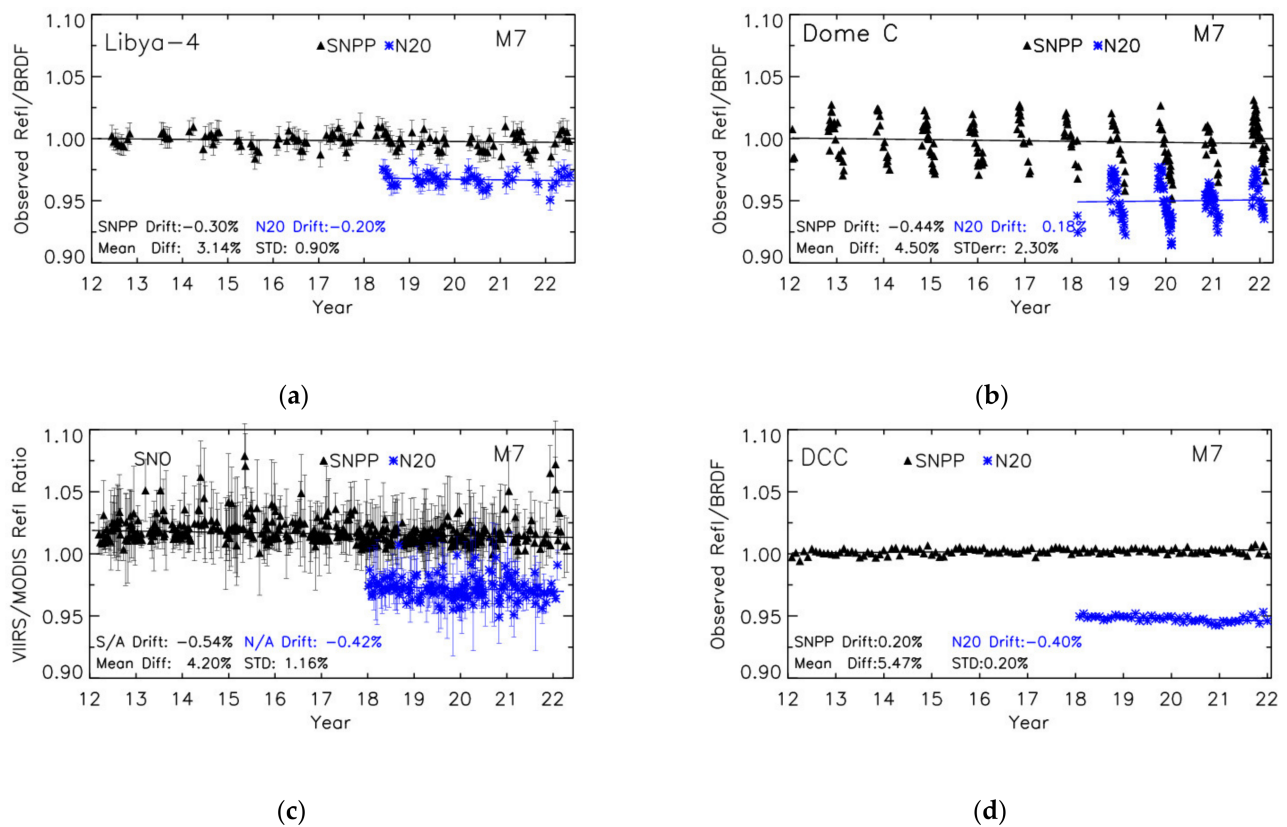
(**a**)　　　　　　　　　　　　　　　　　　　　　(**b**)

(**c**)　　　　　　　　　　　　　　　　　　　　　(**d**)

Figure 5. Normalized reflectance trends for SNPP and NOAA20 VIIRS M7 obtained from the Libya-4 (**a**), Dome C (**b**), SNO with Aqua MODIS (**c**), and DCC (**d**).

One example in the short-wave infrared (SWIR) spectral region, band M8 (1.24 μm), is shown in Figure 6. Results from the Dome C site are excluded due to their large fluctuations in the trends. The SWIR band trends for the Libya-4 site show relatively larger seasonal fluctuations than the VIS and near-IR bands, which is likely due to the combined impact of the surface BRDF and atmospheric absorption. For the DCC approach, the SWIR reflectance is highly dependent on wavelength. As discussed in the methodology, to further reduce seasonal fluctuations, an empirical SWIR band-dependent DCC BRDF model is applied instead of the Hu DCC BRDF, which is effective only for the VIS and near-IR bands. Results indicate there is an excellent stability (<1%) for the SWIR bands. The relative biases between SNPP and NOAA20 SWIR bands are further reduced to approximately 2%, compared with 4% for the near-IR bands and 4–6% in the VIS bands.
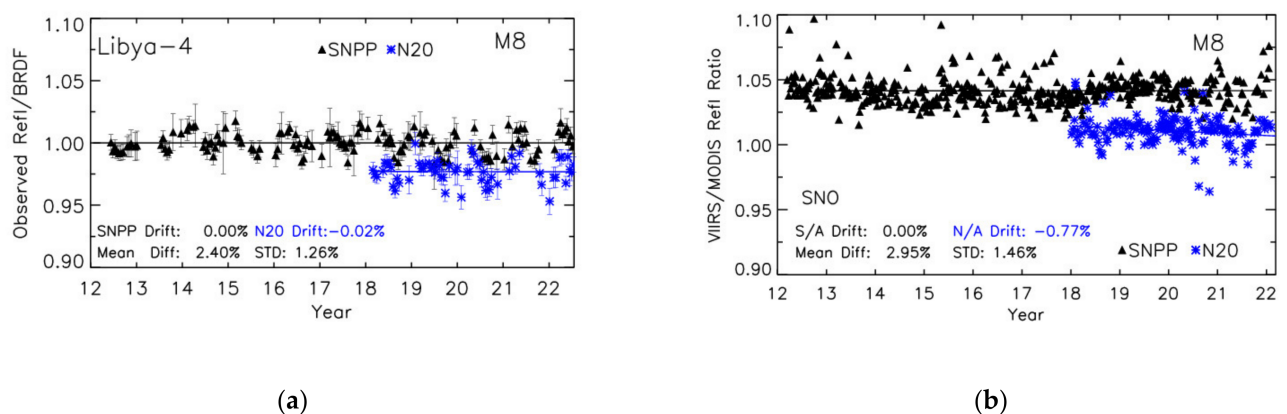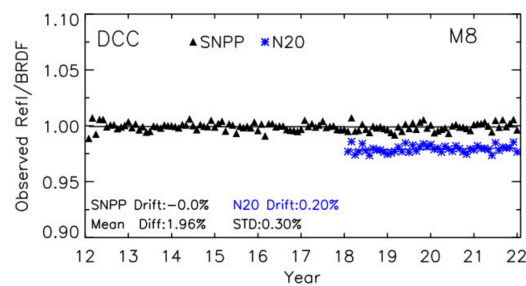

(**a**)　　　　　　　　　　　　　　　　　　　　　(**b**)

Figure 6. *Cont.*

(**c**)

Figure 6. Normalized reflectance trends for SNPP and NOAA20 VIIRS M8 obtained from the Libya-4 (**a**), SNO with Aqua MODIS (**b**), and DCC (**c**).

　　Table 3 lists results of the stability assessment for SNPP VIIRS. Over a ten-year mission period, SNPP VIIRS reflectances show a stability of within 1% for all bands, except for a few VIS bands with more than 1% drifts in the DCC and Dome C results. As discussed for the results of band M3, the drifts occur at the high-radiance level. The stability results from the SNO approach are the relative stability of SNPP VIIRS with respect to Aqua MODIS. A separate stability assessment for Aqua MODIS based on data from 2012 to present is provided in Table 4, indicating the impact of Aqua on SNPP SNO stability, as well as for NOAA20 SNO stability, which is well within 1%, except for Band 8. Results for NOAA20 are shown in Table 5. Bands I1 and M4 for the Dome C site show a drift above 1%, which is also associated with a large standard error. Although its operational period is just over 4 years, the stability results are generally better than SNPP VIIRS. There are no noticeable upward drifts in the NOAA20 results for bands M1 to M5 from the DCC approach.

Table 3. SNPP VIIRS RSB stability from the four vicarious approaches. Results are provided in percentage for drift over the entire mission. Values denoted as ± are the standard error. Those marked "NA" are either not applicable or a data variation.

Band (µm)	M1 0.412	M2 0.445	M3 0.488	M4 0.555	M5 0.672	M7 0.865	M8 1.24	M9 1.378	M10 1.61	M11 2.25	I1 0.640	I2 0.865	I3 1.61
Libya-4	−0.63 ±0.83	−0.67 ±0.78	−0.61 ±0.90	−0.65 ±0.86	−0.37 ±0.64	−0.53 ±0.64	−0.29 ±0.85	NA	−0.29 ±0.50	−0.10 ±1.47	−0.63 ±0.81	−0.49 ±0.69	−0.37 ±0.48
DCC	1.35 ±0.40	0.74 ±0.22	1.70 ±0.30	1.20 ±0.30	0.80 ±0.30	0.20 ±0.20	−0.00 ±0.40	0.60 ±0.80	0.20 ±0.70	0.10 ±0.50	0.60 ±0.30	0.40 ±0.20	0.10 ±0.70
Dome C	1.16 ±0.76	0.66 ±0.81	1.53 ±0.89	2.12 ±1.86	0.98 ±1.31	−0.31 ±1.71	NA	NA	NA	NA	1.61 ±1.90	−0.18 ±1.76	NA
SNO	0.53 ±0.90	−0.23 ±0.74	0.36 ±0.82	0.63 ±0.47	0.39 ±1.54	−0.55 ±0.71	0.02 ±0.99	NA	−0.67 ±2.42	NA	−0.34 ±0.57	−0.62 ±0.71	−0.65 ±2.62

Table 4. Aqua MODIS RSB stability for the Libya-4, Dome C, and DCC approaches. Results are provided in percentage for drift during the 2012–2021 period. Values denoted as ± are the standard error. Those marked "NA" are either not applicable or a data variation.

Band (µm)	B1 0.645	B2 0.858	B3 0.469	B4 0.555	B5 1.24	B6 1.64	B7 2.13	B8 0.412	B9 0.443
Libya-4	0.56 ±0.99	0.50 ±1.05	0.30 ±1.47	0.55 ±1.21	−0.18 ±0.97	−0.07 ±0.83	−0.38 ±1.93	−1.12 ±1.45	−0.31 ±1.50
Dome C	0.18 ±2.08	0.11 ±1.91	0.15 ±0.92	0.58 ±1.05	−0.05 ±2.29	NA	NA	−1.20 ±0.96	−0.47 ±1.25
DCC	−0.26 ±0.85	NA	0.82 ±0.86	0.41 ±0.86	0.01 ±0.60	0.80 ±1.68	0.32 ±2.48	NA	NA

Table 5. NOAA20 VIIRS RSB stability from the four vicarious approaches. Results are provided in percentage for drift over the entire mission. Values denoted as ± are the standard error. Those marked "NA" are either not applicable or a data variation.

Band	M1	M2	M3	M4	M5	M7	M8	M9	M10	M11	I1	I2	I3
Libya−4	−0.09 ±0.71	0.04 ±0.83	−0.48 ±0.91	−0.72 ±0.69	−0.61 ±0.55	−0.75 ±0.65	−0.55 ±0.94	NA	−0.30 ±0.65	−0.60 ±1.60	−0.89 ±0.87	−0.78 ±0.93	−0.24 ±0.62
DCC	−0.86 ±0.85	−1.29 ±0.92	−0.40 ±0.30	−0.50 ±0.40	−0.20 ±0.30	−0.40 ±0.20	0.20 ±0.30	0.30 ±0.80	0.60 ±0.70	0.50 ±0.50	−0.50 ±0.30	−0.54 ±0.64	0.50 ±0.70
Dome C	0.98 ±0.78	0.32 ±0.70	0.71 ±0.92	2.17 ±2.35	0.81 ±1.60	0.18 ±1.81	NA	NA	NA	NA	1.54 ±2.07	0.36 ±1.81	NA
SNO	−0.23 ±1.19	0.20 ±0.80	0.11 ±1.12	0.25 ±0.49	0.35 ±0.96	−0.42 ±0.92	−0.77 ±1.08	NA	−2.11 ±2.12	NA	−0.18 ±0.53	−0.31 ±0.91	−1.45 ±1.91

By comparing the reflectances between SNPP and NOAA20 VIIRS over their data overlapping period, their radiometric calibration consistency is evaluated for each approach. Table 6 shows NOAA20 to SNPP VIIRS reflectance ratios corrected for the band spectral difference. A ratio value lower than one indicates NOAA20 reflectances are lower than SNPP. The ratios are more consistent among the four approaches after the spectral correction. Band M4 has the largest shift in central wavelength between SNPP and NOAA20, the ratios among the different approaches agree within 2% after the spectral correction, compared with differences up to 4% before the correction. The shortest wavelength bands, M1 to M3, show the lowest values of the ratios (less than 1), indicating the largest radiometric biases between NOAA20 and SNPP VIIRS, with magnitudes of the bias from 4 to 7%, depending on band. For the longer wavelength bands in the near-IR and SWIR regions, the biases are approximately 2–3%. One reason for the increased differences in M1 to M3 in the NASA SIPS Collection-2 L1B product is due to a gain adjustment of up to 2% compared with other bands to account for the initial degradation after launch due to UV radiation. Results also show that differences among the different approaches are up to 2.0% and the DCC approach shows the lowest standard errors. This indicates that there are still large uncertainties in the use of these methodologies. It is expected that errors due to existing residual site BRDF impact on the comparison data are approximately 1%, plus an additional 0.5% due to the lack of an observed real-time spectral correction. Similar studies using VIIRS SDR products generated by NOAA CLASS reported the biases on the order of 2% to 4% [18,19]. It should be noted that the VIIRS SDR products, which include calibrated radiance/reflectance and brightness temperatures along with geolocation, are generated using independent calibration algorithms by the NOAA VIIRS SDR calibration/validation team.

Table 6. SNPP and NOAA20 VIIRS RSB comparison. Results are provided in ratio (NOAA20/SNPP). Values in bracket parentheses are the standard error. Those marked "NA" are either not applicable or are excluded due to data variation.

Band	M1	M2	M3	M4	M5	M7	M8	M9	M10	M11	I1	I2	I3
Libya-4	0.925 ±0.011	0.938 ±0.011	0.956 ±0.013	0.966 ±0.011	0.954 ±0.008	0.975 ±0.009	0.976 ±0.013	NA	0.982 ±0.008	0.979 ±0.022	0.970 ±0.012	0.974 ±0.012	0.969 ±0.008
DCC	0.941 ±0.009	0.942 ±0.009	0.948 ±0.003	0.945 ±0.003	0.949 ±0.003	0.960 ±0.002	0.982 ±0.003	0.989 ±0.008	0.988 ±0.007	0.988 ±0.005	0.952 ±0.003	0.970 ±0.007	0.965 ±0.007
Dome C	0.921 ±0.011	0.934 ±0.009	0.950 ±0.011	0.952 ±0.026	0.966 ±0.025	0.975 ±0.023	NA	NA	NA	NA	0.966 ±0.025	0.973 ±0.023	NA
SNO	0.935 ±0.015	0.941 ±0.011	0.956 ±0.014	0.948 ±0.007	0.946 ±0.018	0.968 ±0.017	0.971 ±0.015	NA	0.971 ±0.033	NA	0.967 ±0.008	0.969 ±0.016	0.961 ±0.033

4. Discussion

The cause of the upward drifts for SNPP VIIRS M1 to M5 bands is unclear, and it is considered to be related to on-orbit changes in the nonlinear response coefficients, which are fixed terms used in the RSB calibration algorithm determined from prelaunch measurements. Observations over scenes with high-signal radiance, such as DCC and Dome C surfaces, would magnify the impact of the nonlinearity. Due to the use of inconsistent look up tables for VIIRS C1 L1B before and after 2014, our early results do not indicate the upward drifts in the DCC and Dome C trends.

The reason for the systematic biases between SNPP and NOA20 VIIRS RSB is not clear and a possible cause is likely due to errors in the prelaunch measurements, particularly in the characterization of the SD BRDF. A recent study by Moyer et al. [40] indicates a possibly unaccounted clocking error due to the on-orbit and pre-launch alignment of the SNPP VIIRS SD. The clocking sensitivity measurements were taken for the following VIIRS sensors, such as NOAA20, and results show that such errors can have a significant bias error in the calculation of SD BRF.

While the radiometric differences between SNPP and NOAA20 VIIRS in Table 6 are the means of the time series between 2012 and 2022, the impact of any temporal trends in either of the two instruments is evident, as shown in the stability results of SNPP M1 to M5 for scenes at high radiance, such as DCC and Dome C. The trends or absolute radiometric scales could be changed in future major calibration updates to the L1B products, indicating their relative radiometric differences need to be constantly monitored. The impact of the radiometric differences on downstream up-level products is significant, as shown in the NASA cloud mask (CLDMSK) and cloud-top and optical properties (CLDPROP) products [41] and Deep Blue aerosol products [42]. To achieve geophysical retrieval continuity across multiple sensors, a common heritage sensor, such as Aqua MODIS is used as the reference to derive the SNPP or NOAA-20 VIIRS RSB radiometric adjustments in these products. The CLARREO (Climate Absolute Radiance and Refractivity Observatory) Pathfinder (CPF) mission (to be launched in December 2023) has been designed to take shortwave measurements with unprecedented high accuracy such that they could more rapidly detect radiometric biases and long-term trends than our current on-orbit sensors [43]. This will provide us with the ability to use that unparalleled accuracy to serve as an on-orbit reference for inter-calibration of SNPP and NOAA20 VIIRS RSB and other sensors with reflected solar channels.

5. Conclusions

The two VIIRS instruments onboard the SNPP and NOAA20 satellites have been operating nominally for nearly 10 and 4 years, respectively, providing the global science community with high-quality moderate resolution earth observations in VIS-NIR, SWIR, and IR spectral regimes to facilitate a broad range of scientific studies related to land, atmosphere, cryosphere, and oceans. This study provides an updated assessment of the radiometric stability of the two VIIRS RSB and the calibration consistency between the two instruments. The assessment results are based on the latest operational and publicly available NASA SIPS VIIRS C2 Level-1B products. Several vicarious approaches are used including PICS, such as Libya-4 desert and Dome C, SNO, and DCC. Results indicate that both SNPP and NOAA20 VIIRS reflectances are stable to within 1% over their mission periods for all bands, except for a few short wavelengths from SNPP VIIRS that show more upward drifts in high-radiance conditions. A few bands for the Dome C site with stability above 1% are also associated with larger standard errors. NOAA20 VIIRS reflectances are systematically lower than SNPP by 2 to 4% for most bands. The shortest wavelength bands, M1 to M3, show larger biases than other bands. The NOAA20 to SNPP reflectance ratios are more consistent among the different approaches after correction for the band spectral difference. The results of this study produce useful information about potential impacts on the comparison of downstream science products. It also provides findings that are useful for diagnosing and improving future calibration algorithms.

References

1. Justice, C.O.; Román, M.O.; Csiszar, I.; Vermote, E.F.; Wolfe, R.E.; Hook, S.J.; Friedl, M.; Wang, Z.; Schaaf, C.B.; Miura, T.; et al. Land and cryosphere products from Suomi NPP VIIRS: Overview and status. *J. Geophys. Res. Atmos.* **2013**, *118*, 9753–9765. [CrossRef]
2. Wang, M.; Liu, X.; Tan, L.; Jiang, L.; Son, S.; Shi, W.; Rausch, K.; Voss, K. Impacts of VIIRS SDR performance on ocean color products. *J. Geophys. Res. Atmos.* **2013**, *118*, 10347–10360. [CrossRef]
3. Liu, H.; Remer, L.A.; Huang, J.; Huang, H.-C.; Kondragunta, S.; Laszlo, I.; Oo, M.; Jackson, J.M. Preliminary evaluation of S-NPP VIIRS aerosol optical thickness. *J. Geophys. Res. Atmos.* **2014**, *119*, 3942–3962. [CrossRef]
4. Schueler, C.F.; Clement, J.E.; Ardanuy, P.E.; Welsch, C.; DeLuccia, F.; Swenson, H. NPOESS VIIRS sensor design overview. In Proceedings of the International Symposium on Optical Science and Technology, San Diego, CA, USA, 29 July–3 August 2001; Volume 4483, pp. 11–24. [CrossRef]
5. Murphy, R.E.; Ardanuy, P.; Deluccia, F.J.; Clement, J.E.; Schueler, C.F. The Visible Infrared Imaging Radiometer Suite. In *Earth Science Satellite Remote Sensing*; Springer: Berlin/Heidelberg, Germany, 2006; pp. 199–223. [CrossRef]
6. Cao, C.; De Luccia, F.J.; Xiong, X.; Wolfe, R.; Weng, F. Early on-Orbit Performance of the Visible Infrared Imaging Radiometer Suite Onboard the Suomi National Polar-Orbiting Partnership (S-NPP) Satellite. *IEEE Trans. Geosci. Remote Sens.* **2014**, *52*, 1142–1156. [CrossRef]
7. Xiong, X.; Butler, J.; Chiang, K.; Efremova, B.; Fulbright, J.; Lei, N.; McIntire, J.; Oudrari, H.; Sun, J.; Wang, Z.; et al. VIIRS on-orbit calibration methodology and performance. *J. Geophys. Res. Atmos.* **2014**, *119*, 5065–5078. [CrossRef]
8. Lei, N.; Xiong, X. Products of the SNPP VIIRS SD screen transmittance and the SD BRDFs from both yaw maneuver and regular on-orbit data. *IEEE Trans. Geosci. Remote Sens.* **2017**, *55*, 1975–1987. [CrossRef]
9. Lei, N.; Xiong, X. Determination of the NOAA-20 VIIRS screen transmittance functions with both the yaw maneuver and regular on-orbit calibration data. *Appl. Opt.* **2020**, *59*, 2992–3001. [CrossRef]
10. Xiong, X.; Sun, J.; Fulbright, J.; Wang, Z.; Butler, J.J. Lunar Calibration and Performance for S-NPP VIIRS Reflective Solar Bands. *IEEE Trans. Geosci. Remote Sens.* **2016**, *54*, 1052–1061. [CrossRef]
11. Iona, G.; Butler, J.; Guenther, B.; Graziani, L.; Johnson, E.; Kennedy, B.; Kent, C.; Lambeck, R.; Waluschka, E.; Xiong, X. VIIRS on-orbit optical anomaly: Investigation, analysis, root cause determination and lessons learned. *Proc. SPIE* **2012**, *8510*, 85101C. [CrossRef]
12. Lei, N.; Xiong, X.; Guenther, B. Modeling the Detector Radiometric Gains of the Suomi NPP VIIRS Reflective Solar Bands. *IEEE Trans. Geosci. Remote Sens.* **2015**, *53*, 1565–1573. [CrossRef]
13. Choi, T.; Shao, X.; Cao, C. On-orbit radiometric calibration of Suomi NPP VIIRS reflective solar bands using the Moon and solar diffuser. *Appl. Opt.* **2018**, *57*, 9533–9542. [CrossRef]
14. Xiong, X.; Angal, A.; Chang, T.; Chiang, K.; Lei, N.; Li, Y.; Sun, J.; Twedt, K.; Wu, A. MODIS and VIIRS Calibration and Characterization in Support of Producing Long-Term High-Quality Data Products. *Remote Sens.* **2020**, *12*, 3167. [CrossRef]
15. Mu, Q.; Angal, A.; Twedt, K.; Wu, A.; Xiong, X. MODIS detector differences using deep convective clouds and desert targets. In Proceedings of the SPIE Remote Sensing, Online, 20 September 2020; Volume 11530, p. 115301A. [CrossRef]
16. Sun, J.; Xiong, X.; Lei, N.; Li, S.; Twedt, K.; Angal, A. Ten Years of SNPP VIIRS Reflective Solar Bands On-Orbit Calibration and Performance. *Remote Sens.* **2021**, *13*, 2944. [CrossRef]
17. Wu, A.; Mu, Q.; Angal, A.; Xiong, X. Assessment of MODIS and VIIRS calibration consistency for reflective solar bands calibration using vicarious approaches. In Proceedings of the Sensors, Systems, and Next-Generation Satellites XXIV, Online, 21–25 September 2020; Volume 11530, p. 1153018. [CrossRef]
18. Uprety, S.; Cao, C.; Shao, X. Radiometric consistency between GOES-16 ABI and VIIRS on Suomi NPP and NOAA-20. *J. Appl. Remote Sens.* **2020**, *14*, 032407. [CrossRef]
19. Wang, W.; Cao, C. Evaluation of NOAA-20 VIIRS Reflective Solar Bands Early On-Orbit Performance Using Daily Deep Convective Clouds Recent Improvements. *IEEE J. Sel. Top. Appl. Earth Obs. Remote Sens.* **2020**, *13*, 3975–3985. [CrossRef]
20. Teillet, P.M.; Barsi, J.A.; Chander, G.; Thome, K.J. Prime candidate earth targets for the post-launch radiometric calibration of space-based optical imaging instruments. In Proceedings of the Earth Observing Systems XII, San Diego, CA, USA, 26–30 August 2007; p. 66770S.

21. Chander, G.; Xiong, X.; Choi, T.; Angal, A. Monitoring on-orbit calibration stability of the Terra MODIS and Landsat 7 ETM+ sensors using pseudo-invariant test sites. *Remote Sens. Environ.* **2010**, *114*, 925–939. [CrossRef]

22. Helder, D.; Thome, K.J.; Mishra, N.; Chander, G.; Xiong, X.; Angal, A.; Choi, T. Absolute Radiometric Calibration of Landsat Using a Pseudo Invariant Calibration Site. *IEEE Trans. Geosci. Remote Sens.* **2013**, *51*, 1360–1369. [CrossRef]

23. Doelling, D.R.; Wu, A.; Xiong, X.; Scarino, B.R.; Bhatt, R.; Haney, C.O.; Morstad, D.; Gopalan, A. The Radiometric Stability and Scaling of Collection 6 Terra- and Aqua-MODIS VIS, NIR, and SWIR Spectral Bands. *IEEE Trans. Geosci. Remote Sens.* **2015**, *53*, 4520–4535. [CrossRef]

24. Roujean, J.-L.; Leroy, M.; Deschamps, P.Y. A bidirectional reflectance model of the Earth's surface for the correction of remote sensing data. *J. Geophys. Res.* **1992**, *97*, 20455–20468. [CrossRef]

25. Wu, A.X.; Xiong, D.R.; Doelling, D.; Morstad, A.; Angal, A.; Bhatt, R. Characterization of Terra and Aqua MODIS VIS, NIR, and SWIR Spectral Bands' Calibration Stability. *IEEE Trans. Geosci. Remote Sens.* **2012**, *51*, 4330–4338. [CrossRef]

26. Six, D.; Fily, M.; Alvain, S.; Henry, P.; Benoist, J.-P. Surface characterization of the dome concordia area (Antarctica) as a potential satellite calibration site using spot 4/vegetation instrument. *Remote Sens. Environ.* **2004**, *89*, 83–94. [CrossRef]

27. Wu, A.; Xiong, X.; Cao, C.; Chiang, K.-F. Assessment of SNPP VIIRS VIS/NIR Radiometric Calibration Stability Using Aqua MODIS and Invariant Surface Targets. *IEEE Trans. Geosci. Remote Sens.* **2016**, *54*, 2918–2924. [CrossRef]

28. Wu, A.; Xiong, X.; Cao, C. Using BRDF derived from MODIS observations over Dome C to characterize calibration stability and consistency of POS sensors. *Proc. SPIE* **2009**, *7456*, 745605. [CrossRef]

29. Cao, C.; Weinreb, M.; Xu, H. Predicting simultaneous nadir overpasses among polar-orbiting meteorological satellites for intersatellite calibration of radiometers. *J. Atmos. Ocean. Technol.* **2004**, *21*, 537–542. [CrossRef]

30. Wu, A.; Xiong, X.; Cao, C. Terra and Aqua MODIS inter-comparison of three reflective solar bands using AVHRR onboard the NOAA-KLM satellites. *Int. J. Remote Sens.* **2008**, *29*, 1997–2010. [CrossRef]

31. Doelling, D.R.; Morstad, D.; Scarino, B.R.; Bhatt, R.; Gopalan, A. The Characterization of Deep Convective Clouds as an Invariant Calibration Target and as a Visible Calibration Technique. *IEEE Trans. Geosci. Remote Sens.* **2013**, *51*, 1147–1159. [CrossRef]

32. Bhatt, R.; Doelling, D.R.; Scarino, B.R.; Gopalan, A.; Haney, C.O. An initial assessment of the VIIRS onboard calibration using DCC and desert referenced to the Aqua-MODIS calibration. In *Earth Observing Systems XVIII*; SPIE: San Diego, CA, USA, 2013; Volume 8866, p. 88660K. [CrossRef]

33. Hu, Y.; Wielicki, B.; Yang, P.; Stackhouse, P.; Lin, B.; Young, D. Application of deep convective cloud albedo observations to satellite-based study of terrestrial atmosphere: Monitoring stability of space-borne measurements and assessing absorption anomaly. *IEEE Trans. Geosci. Remote Sens.* **2004**, *42*, 2594–2599.

34. Platnick, S.; Li, J.Y.; King, M.; Gerber, H.; Hobbs, P.V. A solar reflectance method for retrieving the optical thickness and droplet size of liquid water clouds over snow and ice surfaces. *J. Geophys. Res. Earth Surf.* **2001**, *106*, 15185–15199. [CrossRef]

35. Bhatt, R.; Doelling, D.R.; Scarino, B.; Haney, C.; Gopalan, A. Development of Seasonal BRDF Models to Extend the Use of Deep Convective Clouds as Invariant Targets for Satellite SWIR-Band Calibration. *Remote Sens.* **2017**, *9*, 1061. [CrossRef]

36. Bhatt, R.; Doelling, D.R.; Scarino, B.R.; Gopalan, A.; Haney, C.O. Advances in utilizing tropical deep convective clouds as a stable target for on-orbit calibration of satellite imager reflective solar bands. *Proc. SPIE* **2019**, *11127*, 111271H. [CrossRef]

37. Gottwald, M.; Bovensmann, H. *SCIAMACHY—Exploring the Changing Earth's Atmosphere*; Springer: New York, NY, USA, 2011.

38. Scarino, B.R.; Doelling, D.R.; Minnis, P.; Gopalan, A.; Chee, T.; Bhatt, R.; Lukashin, C.; Haney, C. A Web-Based Tool for Calculating Spectral Band Difference Adjustment Factors Derived from SCIAMACHY Hyperspectral Data. *IEEE Trans. Geosci. Remote Sens.* **2016**, *54*, 2529–2542. [CrossRef]

39. Wang, Z.; Xiong, X.; Fulbright, J.; Lei, N. VIIRS day/night band radiometric calibration stability monitoring using the Moon. *J. Geophys. Res. Atmos.* **2017**, *122*, 5616–5624. [CrossRef]

40. Moyer, D.I.; Uprety, S.; Wang, W.; Cao, C.; Guch, I. S-NPP/NOAA-20 VIIRS reflective solar bands on-orbit calibration bias investigation. *Proc. SPIE* **2021**, *11829*, 1182912. [CrossRef]

41. Meyer, K.; Platnick, S.; Holz, R.; Dutcher, S.; Quinn, G.; Nagle, F. Derivation of Shortwave Radiometric Adjustments for SNPP and NOAA-20 VIIRS for the NASA MODIS-VIIRS Continuity Cloud Products. *Remote Sens.* **2020**, *12*, 4096. [CrossRef]

42. Sayer, A.M.; Hsu, N.C.; Bettenhausen, C.; Holz, R.E.; Lee, J.; Quinn, G.; Veglio, P. Cross-calibration of S-NPP VIIRS moderate-resolution reflective solar bands against MODIS Aqua over dark water scenes. *Atmos. Meas. Tech.* **2017**, *10*, 1425–1444. [CrossRef] [PubMed]

43. Wielicki, B.A.; Young, D.F.; Mlynczak, M.G.; Thome, K.J.; Leroy, S.; Corliss, J.; Anderson, J.G.; Ao, C.O.; Bantges, R.; Best, F.; et al. Achieving climate change absolute accuracy in orbit. *Bull. Am. Meteorol. Soc.* **2013**, *94*, 1519–1539. [CrossRef]